



1 Late Neogene terrestrial climate reconstruction of the Central  
2 Namib Desert derived by the combination of U-Pb silcrete and  
3 TCN exposure dating

4 Benedikt Ritter <sup>1\*</sup>, Richard Albert <sup>2,3\*</sup>, Aleksandr Rakipov <sup>2,3</sup>, Fredrik M. van der Wateren <sup>4</sup>, Tibor  
5 J. Dunai <sup>1</sup>, Axel Gerdes <sup>2,3</sup>

6

7 *1 Institute of Geology & Mineralogy, University of Cologne, Germany*

8 *2 Frankfurt Isotope and Element Research Center (FIERCE), Goethe-University Frankfurt, Germany*

9 *3 Institute of Geosciences, Goethe-University Frankfurt, Germany*

10 *4 Philosophical Practice, Cas Oorthuyskade 23, 1087 DP Amsterdam, Netherlands*

11 *\*Equal Contribution - Corresponding Authors*

12

13 *Corresponding authors:*

14 *Benedikt Ritter - [benedikt.ritter@uni-koeln.de](mailto:benedikt.ritter@uni-koeln.de)*

15 *Richard Albert - [AlbertRoper@em.uni-frankfurt.de](mailto:AlbertRoper@em.uni-frankfurt.de)*

16 **Keywords:** Namib Desert, U-Pb dating, groundwater sil-/calcretes, cosmogenic nuclides

17 **Abstract:**

18 The chronology of the Cenozoic, so called ‘Namib Group’ of the Namib Desert is rather poor in  
19 terms of direct radiometric dating. Most of the chronological information is based on the ostrich  
20 shell biochronostratigraphy. The widespread occurrence of calcretes and silcretes in the Namib  
21 Desert makes it possible to date important phases of landscape stability and to retrieve critical  
22 paleoclimatic and -environmental information on desertification and its paleoclimatic variability.  
23 The application of the U-Pb laser ablation dating technique to Plio/Pleistocene sil- and calcretes  
24 provides critical insights into groundwater calcrete formation and climate variability in the  
25 Central Namib. Microscale silcrete formation due to pressure solution by expanding calcrete  
26 cementation provides the opportunity to date multiple phases (multiple generation of silcrete as  
27 growing layers or shells) of silcrete formation and to trace their paleoclimatic and -environmental  
28 fingerprints. Groundwater sil- and calcrete formation occurred during the Pliocene. TCN exposure  
29 ages from flat canyon rim surfaces indicate the cessation of groundwater calcrete formation due  
30 to incision during the Late Pliocene/Early Pleistocene and mark a large-scale landscape  
31 rejuvenation due to climate shifts towards the Pleistocene. This study demonstrates the



32 application of U-Pb laser ablation to groundwater sil- and calcretes in desert environments and  
33 opens up the possibility of dating numerous sedimentary sequences containing sil- and calcretes  
34 in arid environments. In particular, the use of silcretes (as described above) reduces potential  
35 effects of detrital components and bulk-signal measurements by using massive calcretes. Our  
36 study redefines and improves the generally accepted Late Cenozoic chronostratigraphy of the  
37 Namib Desert (Miller, 2008).

## 38 1. Introduction

39 In Namibia, widespread calcretes, together with (spatially) more restricted silcretes, are among  
40 the most auspicious features of the Cenozoic surface cover along deeply incised ephemeral or  
41 fossil drainage systems in terms of their ability to record past environmental change (Miller, 2008;  
42 Candy et al., 2004; Summerfield, 1983a; Van Der Wateren and Dunai, 2001; Ward, 1987). As well  
43 as being an important component in explaining the generally low denudation rates due to their  
44 protective function (Stokes et al., 2007; Nash and Smith, 1998), these sil- and calcretes also  
45 indicate relatively long periods of landscape and climate stability during their formation.

46 In general, calcretes are thought to form under semi-arid to arid conditions, with varying  
47 interpretations and associations with specific precipitation ranges (Goudie, 2020; Summerfield,  
48 1983a; Alonso-Zarza, 2003). The formation of calcretes is largely dependent on the local climate  
49 and the availability of calcium and carbonate ions in the system, produced by weathering and  
50 leaching in the catchment. Various models have been proposed to explain the different types of  
51 calcrete (pedogenic, non-pedogenic, Goudie, 2020). In this study, we will mainly focus on the  
52 non-pedogenic, groundwater-related calcrete formation, based on the *per-ascensum* hypothesis  
53 (Goudie, 1996; Goudie et al., 2015). One of the most prominent calcrete formations is related to  
54 calcretes capping the Karpfenkliff Conglomerate of the Kuiseb Canyon in the Central Namib and  
55 the Kamberg Calcrete Formation (Fig. 1, Ward, 1987). Secondary silcrete formation by pressure  
56 solution and reprecipitation was synchronous with calcrete formation in the Karpfenkliff  
57 conglomerates. It consists of microscale silcrete with discrete multiple layers of silcrete  
58 encrusting quartz clasts within this formation. The Karpfenkliff Conglomerate overlies the  
59 Tsondab Sandstone and was probably deposited in a proto-Kuiseb and a proto-Gaub valley (Ward  
60 et al., 1983; Miller, 2008; Ward, 1987).

61 Calcretes in the central Namib are thought to be at least Early Pleistocene to Pliocene in age (Ward,  
62 1987; Miller, 2008). Common dating techniques used to date calcretes are radiocarbon  $^{14}\text{C}$ , U/Th  
63 disequilibrium, or solution U-Pb. Calcrete U-Pb laser ablation has recently been used to provide  
64 critical chronological information on the age-depth relationship of the calcretized sediments from  
65 the Etosha Pan (Houben et al., 2020). However, the dating of calcretes using the U-Pb system may



66 be influenced/biased by detrital components from the source area of the leached carbonates. The  
67 rather slow growth rate makes it difficult to obtain individual ages from multiple generations of  
68 calcrete formation when using the bulk sampling approach for solution U-Pb dating, as it is  
69 affected by the 'nugget' effect (Branca et al., 2005). Although calcrete formation clearly pre-dates  
70 the major canyon incision that can be dated using TCN exposure dating, calcrete formation  
71 post-dates sediment deposition and is not age-equivalent to the host sediments. However, the  
72 time lag between sediment deposition and calcrete formation may be negligible for any expected  
73 age in the range of several millions of years. To avoid contamination by detrital components from  
74 the catchment and to date multiple stages of sil-/calcrete formation, syndepositional (with  
75 calcrete formation), microscale silcretes produced by the secondary effect of calcrete formation,  
76 pressure solution and re-precipitation in the proximity (pressure shadow) might be a valuable  
77 target.

78 Evidence for climate change and major landscape change, as well as the reliability of dating of  
79 Plio/Pleistocene sediments in the Namib, is relatively poor and not well constrained, and in part  
80 shows discrepancies between different dating techniques and interpretations (Miller, 2008; Van  
81 Der Wateren and Dunai, 2001; Goudie and Viles, 2014). In Namibia, calcretes and silcretes  
82 commonly form prominent landscape features (i.e., cliffs) along deeply incised ephemeral or fossil  
83 drainage systems (Miller, 2008; Van Der Wateren and Dunai, 2001; Ward, 1987). The (relative)  
84 chronology of these fossil duricrusts is the backbone of the (late) Cenozoic chronostratigraphy of  
85 the Namib Desert ('Namib Group' of Miller, 2008) and past climate reconstructions (Miller, 2008,  
86 and references therein). A major weakness of this chronostratigraphy is its absolute chronology:  
87 essentially all early Quaternary to mid-Miocene continental deposits in the Namib Desert are  
88 dated with ostrich shells (Miller, 2008) or are age-correlated with deposits dated with such shells  
89 (Miller, 2008). The catch is that only the oldest shells (Aepyornithoid, Senut, 2000) are 'dated' to  
90 16-20 Ma (Pickford et al., 1999), whereas the ensuing eight ostrich species are arbitrarily assigned  
91 to 2 to 3 Myr long periods (Senut, 2000) without any direct age control. The ostrich shell  
92 biostratigraphy provides a valuable relative chronology, but its use in its current form as an  
93 absolute chronology remains unverified for the time < 16 Ma. Consequently, the generally  
94 accepted Late Cenozoic chronostratigraphy of the Namib Desert (Miller, 2008) requires  
95 verification.

96 The use of TCN exposure dating in the Namib Desert has grown in recent years, demonstrating  
97 that this method is a reliable way to measure landscape change (Van Der Wateren and Dunai,  
98 2001; Vermeesch et al., 2010; Stone, 2013; Bierman and Caffee, 2001). According to Van Der  
99 Wateren and Dunai (2001), major changes in the Namib Desert, i.e. rejuvenation of the landscape  
100 by intermittent fluvial phases during the predominant arid to hyperarid climate, indicate major  
101 changes during the Plio-/Pleistocene. However, there are doubts about the interpretation of the

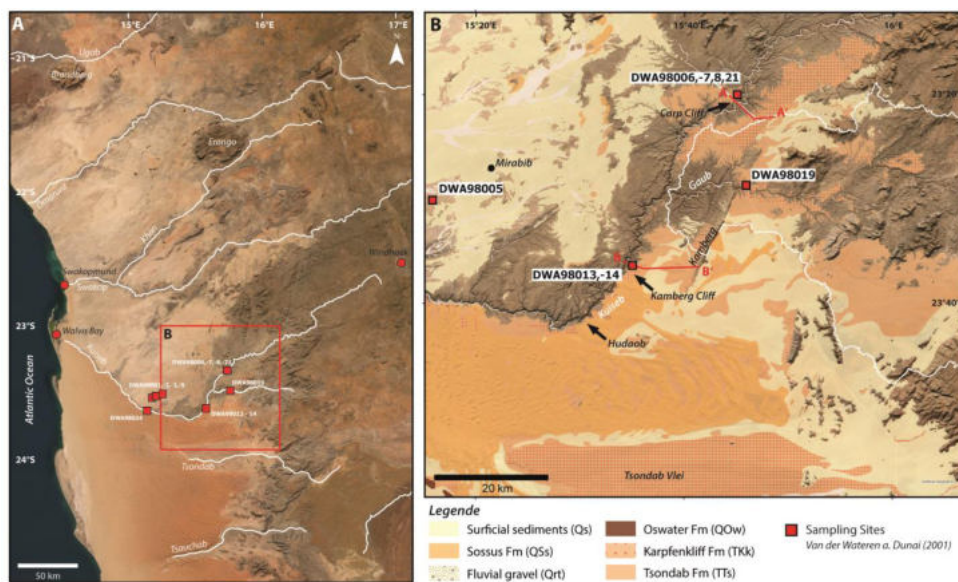


102 exposure ages in relation to the underlying deposited sediments (Miller, 2008). The dating of  
103 groundwater connected sil- and calcretes beneath the surfaces sampled for TCN exposure dating  
104 allows to verify the resulting TCN exposure ages. Furthermore, the combination of both dating  
105 techniques can be used to build a robust chronology of landscape change during the evolution and  
106 intensification of arid conditions in the Namib Desert.

107 Here we present the new application of U-Pb laser ablation to groundwater silcretes from the  
108 Namib Desert in combination with re-measured TCN exposure ages from the Karpfenkliff and  
109 nearby equivalent sites. Laser ablation U-Pb dating of multiple microscale silcrete layers from the  
110 Karpfenkliff Conglomerate Formation indicates groundwater cal-/silcrete formation during the  
111 Pliocene. Re-measured surface clasts from Van Der Wateren and Dunai (2001) confirm and  
112 substantiate the interpretation of a major landscape rejuvenation of the Central Namib during the  
113 Plio-/Pleistocene transition. The combination of the two dating techniques allows a robust  
114 chronological reconstruction of landscape evolution and the paleoclimate transition to  
115 increasingly arid conditions in the central Namib Desert.

## 116 2. Sampling Site and Samples

117 The central Namib Desert, between the Atlantic Ocean to the west and the Great Escarpment to  
118 the east, is a relatively flat landscape with numerous dispersed inselbergs and locally deeply  
119 incised canyons formed by ephemeral rivers such as the Kuiseb or Swakop (Fig. 1). Our study  
120 focuses on the Kuiseb River canyon in the central Namib. The ephemeral Kuiseb River marks the  
121 prominent boundary between the stone desert in the north and the Namib Sand Sea to the south.  
122 The Kuiseb River receives its water from precipitation in the Great Escarpment to the east, with  
123 mean annual rainfall of 200-450 mm/yr (Ward, 1987; Jacobson et al., 1995). Annual floods of the  
124 Kuiseb River clean its bed of all sand transported from the Namib Sand Sea to the south. They only  
125 reach the sea during exceptionally high floods (Van Der Wateren and Dunai, 2001). The Kuiseb  
126 River forms a distinctive deep and partly narrow canyon, which is up to 250 m deep and only  
127 1000 m wide at its deepest part (Fig. 1, 2). The recent course of the Kuiseb River is south-  
128 southwest to Hudaob, where it is thought to have been redirected north-west by the activity of the  
129 Namib Sand Sea (Miller, 2008). Prior to this deflection, the Proto-Kuiseb River may have flowed  
130 westwards, as indicated by numerous outcrops within the interdune valleys of the Namib Sand  
131 Sea (Fig. 25.18 Vol. 3 in Miller, 2008; Ward, 1987; Lancaster, 1984).



132

133 *Fig. 1: (A) Overview map of the Central Namib Desert based on World Imagery (Earthstar*  
134 *Geographics (TerraColor NextGen) imagery, ArcGIS Pro Version 3.1.0). Major drainage systems are*  
135 *shown in white. Red rectangle indicates the study area. Red squares indicate sampling sites of Van*  
136 *Der Wateren and Dunai (2001). Topographic profiles in Fig. 2 are marked as red lines. (B) Study area*  
137 *(Earthstar Geographics (TerraColor NextGen) imagery, ArcGIS Pro Version 3.1.0) including mapped*  
138 *geology by the Geological Survey of Namibia (Geological Survey of Namibia, 2016). Relevant*  
139 *geological formations are shown covering the Cenozoic sediment succession of the Central Namib*  
140 *(Namib Group). Red squares indicate sampling sites from Van Der Wateren and Dunai (2001). The*  
141 *sub-catchment of the Gaub River is shown in white.*

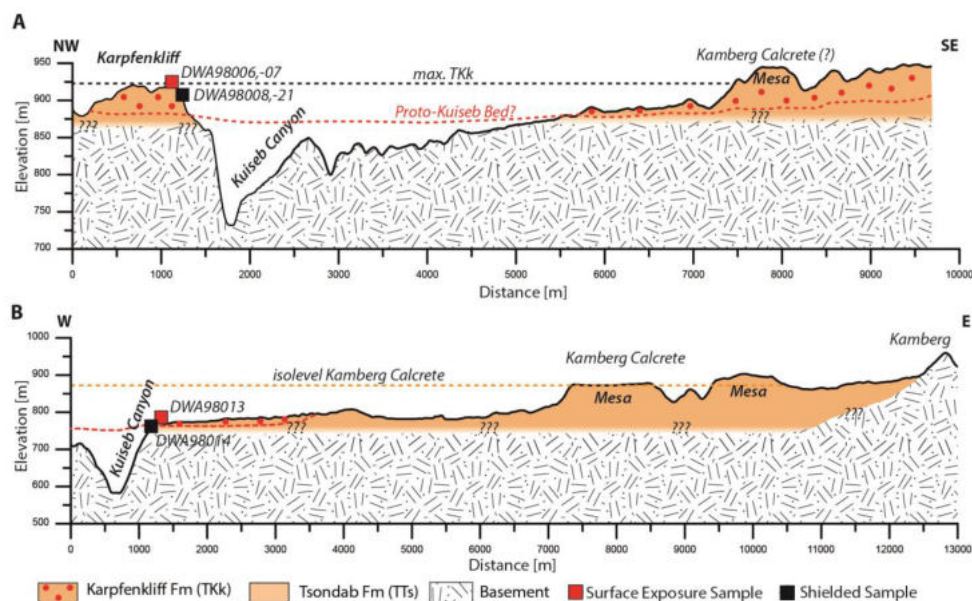
#### 142 Sediment Succession Kuiseb Canyon

143 The outcrop sequence along the Kuiseb canyon in our study area comprises up to 100 m of  
144 sedimentary units (Fig. 2), consisting of basal breccias, Precambrian basement, and solidified  
145 aeolian sands assigned to the Tsondab Sandstone Formation, overlain by calcretized  
146 coarse-grained conglomerates, called the Karpfenkliff Conglomerate Formation (Ward, 1987).  
147 Well-preserved terraces, resistant to weathering due to calcretization, are exposed at the rim of  
148 the canyon (Fig. 3).

149 The Tsondab Sandstone Formation rests on the Namib Unconformity Surface (NUS, Ward, 1987;  
150 Miller, 2008), and is the oldest and first terrestrial Cenozoic deposit in the Central Namib (Ward,  
151 1987; Miller, 2008), covering large areas of the Central Namib (Fig. 1, 2). The Tsondab Sandstone  
152 Formation consists predominantly of cemented aeolianites (Miller, 2008; Ward, 1987) and is  
153 regarded as the precursor of the recent Namib Sand Sea (Ollier, 1977). The Tsondab Sandstone  
154 Formation is thought to have been deposited under predominantly arid conditions (Ward, 1987),



155 between 20-16 Ma and 5 Ma based on the biostratigraphy of Struthious eggshells (Namoris  
156 Oshanai, *Struthio Karinagarabensis*, Ward and Corbett, 1990; Pickford et al., 1995; Senut, 2000).



157

158 *Fig. 2: (A) Cross-sections of the Karpfenkliff and (B) Kamberg Cliff based on SRTM data*  
159 *(created using ArcGIS Pro 3.1.0). Spatial information on geological units was extrapolated from*  
160 *mapped geology (Geological Survey of Namibia, 2016). Samples were collected from the surface of the*  
161 *Karpfenkliff (DWA980006,07) and from the subsurface at the canyon outcrop (DWA980008, -*  
162 *21). The identical sampling approach was used on the Kamberg Cliff, by sampling exposed quartz*  
163 *clasts (DWA98013) and shielded clasts (DWA98014). The shielded quartz clasts were used to*  
164 *investigate and date secondary micro-scale silcrete layers attached to quartz clasts. Due to the*  
165 *unknown fluvial topography of the Proto-Kuseib, the profile is just an approximation. The occurrence*  
166 *of the Karpfenkliff Conglomerate Formation (TKk) is used from the geological map, however, its*  
167 *outcrop condition in profile A in the eastern sector remains speculative. The exact transition from*  
168 *the underlying Tsondab Sandstone (TTs) to the Karpfenkliff Conglomerate Formation is unclear and*  
169 *is approximated. The elevation of the Kamberg Calcrete from its key position is marked in B and to*  
170 *illustrate the potential discrepancy between the two formations.*

#### 171 Proto-Kuseib Incision and aggradation of the Karpfenkliff Conglomerate Formation

172 The Karpfenkliff Conglomerate Formation (TKk, Ward, 1987) overlies the Tsondab Sandstone  
173 Formation and was deposited in a proto-Kuseib and proto-Gaub River valley, a tributary of the  
174 Kuseib River (Fig. 1, 2). Pre-depositional incision of the Kuseib and Gaub rivers probably occurred  
175 during a wetter phase (Ward, 1987; Miller, 2008). The incision excavated a broad shallow valley  
176 and eroded the semi-consolidated Tsondab Sandstone without eroding the underlying  
177 Pre-Cambrian Damaran schists (Ward, 1987; Miller, 2008). The Karpfenkliff Conglomerate  
178 Formation consists of a medium- to fine-grained, sand-sized matrix of angular to subrounded



179 clasts (Fig. 3, Ward, 1987; Miller, 2008). Clasts are rounded to well-rounded with numerous  
180 occurring percussion marks (Ward, 1987; Van Der Wateren and Dunai, 2001). The Karpfenkliff  
181 Conglomerate Formation thins to the west, indicating a depositional wedge (Miller, 2008). The  
182 thickest accumulations are found at the foothills of the Great Escarpment (~ 60 m, Miller, 2008),  
183 decreasing to ~ 40 m (Ward, 1987) in the upper Gaub Valley, 20-30 m at the Karpfenkliff, and  
184 thinning to ~5 m at Gomkaeb (Ward, 1987; Miller, 2008). Deposition took place in a wide, shallow,  
185 braided river system (Ward, 1987; Miller, 2008), presumably during an intermittent pluvial phase  
186 despite prevailing arid conditions and synchronous with the deposition of the Tsondab aeolianites  
187 (Ward, 1987). Equivalent gravels in the Tsondab, Tsauchab and Swakop rivers are assigned to the  
188 Karpfenkliff Conglomerate Formation (Miller, 2008). The conglomerate is cemented by a massive  
189 groundwater calcrete that has caused significant volume expansion (Miller, 2008). The source  
190 area of the carbonate ions is thought to be the outcropping and eroding Precambrian Nama Group  
191 in the headwaters of the Kuiseb River and is therefore authogenic in origin. Calcretization caused  
192 secondary precipitation of microscale silcrete by pressure solution and local re-precipitation.

193 The Karpfenkliff Conglomerate Formation is age-correlated with the occurrence of *Diamantornis*  
194 *corbetti* in the Tsondab Aeolianites at Elim (Pickford and Senut, 2000; Miller, 2008), implying a  
195 younger age of *Diamantornis corbetti* than 14-15 Ma, equivalent to the age of the Arries Drift  
196 Formation (Miller, 2008). Youngest deposition age (prior to  $2.81 \pm 0.11$  Ma) was proposed by Van  
197 Der Wateren and Dunai (2001) based on  $^{21}\text{Ne}$  exposure dating of abandoned surfaces of the  
198 Kuiseb River. The latter indicates the minimum depositional age for the last remnants of any  
199 fluvial transport and deposition of the Karpfenkliff Conglomerate Formation. Although this age is  
200 controversial according to Miller (2008, page 25-27) based on the ostrich shell biostratigraphy, it  
201 clearly indicates the onset of incision by the recent Kuiseb River.

#### 202 Calcrete within Karpfenkliff Formation and Tsondab Sandstone - Kamberg calcrete formation

203 The Kamberg Calcrete is described as a pedogenic calcrete up to 5 m in thickness (Miller, 2008;  
204 Ward, 1987; Yaalon and Ward, 1982). According to Miller (2008), it cements the upper  
205 Karpfenkliff Conglomerate Formation in places, as well as the Tsondab Sandstone, which covers a  
206 large area east of Homeb in the Kuiseb River (Miller, 2008; Ward, 1987; Yaalon and Ward, 1982).  
207 The Kamberg Calcrete, as well as equivalent calcretes in the study area, represent the surface  
208 predating the recent canyon incision of the Kuiseb and Gaub rivers. They are used as an important  
209 stratigraphic marker horizon in the Cenozoic 'Namib Group' (Miller, 2008; Ward, 1987). Whether  
210 the Kamberg Calcrete is identical to the calcrete of the Karpfenkliff can be questioned (Fig. 2). The  
211 pedogenic Kamberg Calcrete may be transitional to the groundwater calcrete found at the  
212 Karpfenkliff and therefore be syndepositional. If the Kamberg Calcrete at the key site at Kamberg  
213 correlates with the Kamberg Cliff and the Carp Cliff at Kuiseb canyon, this would imply that it is



214 stratigraphically equivalent to or younger than the groundwater calcrete cementing the  
215 Karpfenkliff Conglomerate Formation (Fig. 2). A late Miocene age has been suggested for the  
216 evolution of the Kamberg Calcrete (Yaalon and Ward, 1982; Ward, 1987). The calcrete is thought  
217 to have been formed under semi-arid conditions during a relatively long period of landscape  
218 stability (Goudie et al., 2015; Ward, 1987), with seasonal precipitation of potentially 350-450 mm  
219 in the headwaters, decreasing drastically to the west (Ward, 1987).

220 A clear differentiation between the Kamberg Calcrete and any calcretes overlying and/or within  
221 the Karpfenkliff Conglomerate Formation is difficult. The Kamberg Calcrete is not specifically  
222 mapped in the published geological maps (Geological Survey of Namibia, 2016). For our study, we  
223 focused on near-surface clasts with silcrete at the Karpfenkliff. The clear spatial and evolutionary  
224 differentiation, as well as the connection between the two, should be the focus of future research  
225 to use their occurrence as a marker horizon in the Central Namib.

#### 226 Kuiseb Incision – Phase of landscape rejuvenation

227 The incision of the Kuiseb River (and other adjacent rivers such as the Swakop to the north) is  
228 thought to have begun at the end of the Neogene, synchronous with other major river systems in  
229 South Africa (Ward, 1987; King, 1951; Partridge and Maud, 1987; Korn and Martin, 1957). The  
230 recent incision was able to cut deeply into the Karpfenkliff Conglomerate Formation, the Tsondab  
231 Sandstone Formation and also into the Pre-Cambrian Damaran schists (Miller, 2008; Van Der  
232 Wateren and Dunai, 2001; Ward, 1987), forming a V-shaped valley and the famous Kuiseb canyon  
233 (Fig. 3). The transition from the aggradation of the Karpfenkliff Conglomerate Formation and the  
234 formation of calcretes, to the degradation and incision of the recent Kuiseb, Gaub and Swakop  
235 rivers is thought to be related to either a tectonic- (King, 1955; Ward, 1987; Korn and Martin,  
236 1957) or climatic control and forcing (Van Der Wateren and Dunai, 2001; Richards and Richards,  
237 1987; Weissel and Seidl, 1998).

#### 238 Detailed sampling sites and sampling

239 We consider that the calcrete at our sampling sites (Karpfenkliff, and Kamberg Cliff, Fig. 1, 2, 3)  
240 was formed primarily by groundwater interaction, due to its direct location near the present-day  
241 Kuiseb canyon. We used sampled and dated (in-situ  $^{21}\text{Ne}$ ) surface quartz clasts from Van Der  
242 Wateren and Dunai (2001), from abandoned exposed surfaces and shielded clasts from several  
243 metres below the surface. Details of the sampling procedure and sampling sites are given in Van  
244 Der Wateren and Dunai (2001). For this study we concentrated on surface quartz clasts from the  
245 Carp Cliff (DWA98006, -07, -08, -21) and the Kamberg Cliff (DWA98013, -14) for re-measurement  
246 of cosmogenic  $^{21}\text{Ne}$  concentrations. Eight quartz clasts from the Carp Cliff with visible silcrete





247 cementation were prepared for U-Pb laser ablation. The following descriptions are taken from  
248 Van Der Wateren and Dunai (2001) and partly adapted for additional samples.



249

250 *Fig. 3: Outcrop image compilation. (A) From Van Der Wateren and Dunai (2001) Kamberg Cliff, ~15 m of*  
251 *Karpfenkliff Conglomerates overlying ~15 m of Tsondab Sandstones. (B) Carp Cliff (Field Campaign 2018). (C)*  
252 *Close-up of the calcrete-cemented Karpfenkliff Conglomerate Formation. Rounded quartz clasts float in a*  
253 *matrix-supported fabric which is cemented by calcrete. Some clasts are fractured by volume expansion of the*  
254 *calcrete, resulting in pressure solution and formation of micro-scale silcrete. (D) Surface of the calcrete*  
255 *cemented Karpfenkliff.*

256 Carp Cliff (Kuisseb highest terrace)

257 DWA98006-07 (Site 6) is located on the horizontal upper surface of a mesa-shaped terrace  
258 remnant 500 m west of the 200 m deep Kuisseb Canyon (Fig. 1, 2). The terrace has a surface area  
259 of ~5 km<sup>2</sup> and is surrounded by steep, locally vertical and overhanging cliffs, which to the east and  
260 south are nearly 50 m in height. The terrace surface consists of a desert pavement of mainly quartz  
261 pebbles overlying up to 15 cm of sandy silt. This is underlain by 10–25 m of calcretized pebble  
262 and boulder conglomerates of the Karpfenkliff Conglomerate Formation (Fig. 3). Van Der Wateren  
263 and Dunai (2001) collected 40 rounded (DWA98007) and (sub-)angular pebbles (DWA98006)  
264 with diameters between 2 and 6 cm. The site is located at the top of the mesa and is almost  
265 horizontal, so that post depositional transport of the sampled pebbles by the Kuisseb River or local  
266 precipitation can be excluded.



267 DWA98008 and DWA980021 (Site 7 and 19) are located next to small gullies running from the  
268 north side of the Carp Cliff mesa. At these sites, we collected shielded samples from 5 m below the  
269 terrace surface. Van Der Wateren and Dunai (2001) sampled rounded pebbles from the ceilings  
270 of overhangs to ensure that the measured  $^{21}\text{Ne}$  concentrations were derived only during hillslope  
271 and fluvial transport to their present site and not from subsequent exposure at the sampling site.

#### 272 Kamberg Cliff (Kuseib highest terrace)

273 DWA98013 and DWA980014 are from a terrace on the Karpfenkliff Conglomerate Formation  
274 immediately adjacent to the nearly 250 m deep Kuseib Canyon, 30 km downstream of Carp Cliff  
275 (Fig. 1, 2, 3). The terrace surface is very similar to that of Carp Cliff, with a desert pavement of  
276 pebbles and cobbles on a sandy silt overlying 25 m of calcretized conglomerates. The Karpfenkliff  
277 Conglomerates rest on 30–50 m of the Tsondab Sandstone Formation, which forms the bulk of the  
278 cliff adjacent to the canyon. DWA98013 sampling site is on the horizontal surface of the terrace,  
279 where we sampled angular pebbles. At DWA98014, rounded pebbles (DWA98014) were sampled  
280 from the ceiling of an overhang in the cliff face 6 m below.

### 281 **3. Formation of Calcretes and microscale silcretes**

282 In general, two types of calcretes can be differentiated, pedogenic and groundwater calcretes  
283 (Alonso-Zarza and Wright, 2010), following the *per descensum* or the *per ascensum* evolutionary  
284 model (Goudie, 2020). They occur preferentially in arid to semi-arid climates (Alonso-Zarza,  
285 2003; Candy and Black, 2009; Goudie, 2020). Specific climatic and environmental conditions are  
286 required for calcrete formation; (1) precipitation in the headwater/source area to promote  
287 carbonate dissolution, (2) intermittent or seasonal precipitation downstream favour  
288 groundwater systems capable of (3) causing high evaporation and evapotranspiration for  
289 chemical precipitation of carbonate (Mann and Horwitz, 1979). Calcrete formation is dependent  
290 on the supply of carbonate ions leached from the drainage bedrock. In this study we focus on  
291 groundwater calcretes formed along the Kuseib- and Gaub rivers. Groundwater calcretes form at  
292 or above shallow groundwater tables/aquifers (Mann and Horwitz, 1979; Netterberg, 1969) and  
293 do not require subaerial exposure, although shallow contacts and stable surfaces favour the  
294 evolution of groundwater calcretes (Alonso-Zarza, 2003). They were originally called ‘valley  
295 calcretes’ (Butt et al., 1977) because of their relationship with drainages. Groundwater calcretes  
296 are rather restricted to local drainages, although groundwater calcretes can have lateral extents  
297 of more than 100 km long and 10 km wide, depending on the drainage topography (Mann and  
298 Horwitz, 1979). Groundwater calcretes do not have characteristic features compared to  
299 pedogenic calcretes and are rather massive bodies (Alonso-Zarza, 2003). The permeability  
300 (coarse channel sediments) of the host rock favours their formation (Alonso-Zarza and Wright,  
301 2010). Calcretes have been frequently used to obtain paleo precipitation information, but the



302 specific ranges are still under discussion. The upper limit may be between 600 and 1000 mm/yr  
303 (Mack and James, 1994). The lower limit may be as low as 50 mm/yr (Goudie, 1973; Retallack,  
304 1994).

305 Silcretes can form as duricrust due to the accumulation of secondary silica within a soil or host  
306 rock (Milnes and Thiry, 1992; Summerfield, 1983a). Prominent examples include silcretes from  
307 Australia (Milnes et al., 1991; Taylor and Eggleton, 2017) or the Kalahari Desert (Summerfield,  
308 1983b; Nash and Shaw, 1998). In this study, we focus on microscale silcretes, which are formed  
309 by pressure solution (Mcbride, 1989; Rutter, 1983; Sorby, 1863; Wilson, 2020) due to calcrete  
310 cementation and volume expansion within the host rock or sediment, and therefore cannot be  
311 directly compared to the commonly used term 'silcrete'. Microscale silcrete formation is therefore  
312 thought to be linked to paleo-environmental and climatic conditions favourable to calcrete  
313 formation. Calcretization involves the precipitation of  $\text{CaCO}_3$  within the pore spaces of the host  
314 rock or sediment, causing significant volume expansion. A secondary effect of this process is to  
315 increase the differential pressure within the host rock or sediment, causing clast shattering,  
316 relocation and pressure solution at intergranular contacts (Sorby, 1863; Rutter, 1983). Increased  
317 stress at grain boundaries and intergranular contacts leads to dissolution, e.g., silica mobilisation.  
318 Mobilized solutions migrate to regions of lower compressive stress, the 'pressure shadow', to  
319 reprecipitate. Theoretically, depending on the remaining pore space, multiple pressure solution  
320 and reprecipitation cycles can be archived in the host rock as multiple silcrete layers or shells  
321 attached to quartz clasts.



## 322 4. Methods

### 323 Raman Spectroscopy

324 Raman spectra were collected with up to 1300 wavenumber ( $\text{cm}^{-1}$ ), using a WITec alpha 300R  
325 confocal Micro-Raman microscope, at the Goethe University Frankfurt (GUF). The objective used  
326 was 50x, an excitation laser of 532 nm (using 10 mW laser power before the objective), and  
327 spectra integration time of 0.2 s with 5 accumulations in total. Maps ( $400 \times 400 \mu\text{m}^2$ ) were  
328 performed applying a step size of  $1.3 \mu\text{m}$  with a holographic grating of 600 grooves  $\text{mm}^{-1}$ . The  
329 instrument was calibrated using an Ar-Hg spectral lamp and was checked regarding its  
330 performance before the measurements with respect to the  $1300 \text{ cm}^{-1}$  line of silicon. The spectrum  
331 of each sample layer was confirmed at several locations on the same layer. Raman spectra of  
332 reference compounds are found in the Ruff database (<https://rruff.info/>).

### 333 Dating of Silcretes – U-Pb Laser Ablation ICP-MS

334 Quantifying the timing and duration of calcrete formation is quite difficult. Clear stratigraphic  
335 relationships with the overlying and underlying sediments are not straightforward, as  
336 groundwater calcrete, for example, forms within sediments deposited close to the surface.  
337 Numerous studies propose only relative age controls and estimates of the formation time, such as  
338 the application of the ostrich shell biochronostratigraphy used for the Namib Group (Pickford and  
339 Senut, 2000; Senut, 2000; Miller, 2008). Many attempts have been made to date deposits and  
340 determine formation times using radiocarbon  $^{14}\text{C}$  (e.g. Geyh and Eitel, 1997), U/Th (Kelly et al.,  
341 2000; Candy et al., 2004; Candy and Black, 2009) or U-Pb dating (Rasbury and Cole, 2009; Houben  
342 et al., 2020). The latter dating technique allows the investigation of much older calcretes than  
343 radiocarbon  $^{14}\text{C}$  or U/Th.

344 Silcretes are enriched in U relative to calcretes and occur in most soils in arid and semi-arid  
345 environments. Uranium decays to Pb isotopes through a chain of intermediate daughter isotopes,  
346 and ages of thousands- to millions-of-years-old samples can be estimated using parent-daughter  
347 pairs  $^{238}\text{U}$ - $^{206}\text{Pb}$ ,  $^{235}\text{U}$ - $^{207}\text{Pb}$ ,  $^{234}\text{U}$ - $^{230}\text{Th}$ , and  $^{238}\text{U}$ - $^{234}\text{U}$ . The use of a particular isotope pair depends  
348 on how old the sample is compared to the half-life of the selected radioactive isotope within the U  
349 decay chain (Neymark, 2011; Neymark et al., 2002, 2000). Considering that the samples are 2.85  
350 Ma old or older (Van Der Wateren and Dunai, 2001), the U-Pb method using the parent-daughter  
351 pairs  $^{238}\text{U}$ - $^{206}\text{Pb}$  and  $^{235}\text{U}$ - $^{207}\text{Pb}$  was chosen to date the samples in this work.

352 Many studies attempting to date massive cal-/silcretes are hampered by the dilution or averaging  
353 effect of bulk analysis and by bias from non-carbonate detrital minerals or secondary  
354 reprecipitated carbonate due to diagenesis. The “limestone dilution effect” (as a result of  
355 contamination with detrital carbonate components of the host rock, Alonso-Zarza, 2003) or the



356 “averaging effect” (averaging of different phases of mineral precipitation, Candy and Black, 2009;  
357 Neymark et al., 2000) are minimised (or even avoided) by the higher spatial resolution of laser  
358 ablation compared to bulk analysis techniques. The possible effect of detrital components (e.g.  
359 Zircon or clay minerals) on the U-Pb analyses is also neglected, as the signals from these inclusions  
360 can be filtered out of the time-resolved analyses.

361 The conventional method of calculating U–Pb isotope dates assumes that all intermediate  
362 daughter isotopes in the  $^{238}\text{U}$  and  $^{235}\text{U}$  decay chains were in secular equilibrium at the time of  
363 formation (i.e. the radioactivity of all daughter isotopes was equal to that of the parent, Neymark,  
364 2014). This is not necessarily true for calcretes and silcretes due to differences in the geochemical  
365 behaviour of parent and daughter elements. The silcretes dated in this study are sufficiently old  
366 (> c. 2.85 Ma) to have achieved secular equilibrium (at present), and therefore allowing all its  
367 initial excess of daughter isotopes to decay, or their initial depletion to replenish (i.e. their activity  
368 ratios to be equal to 1). This does not allow any initial excess or depletion of daughter isotope to  
369 be measured, making it difficult to correct for potential bias in the  $^{206}\text{Pb}^*/^{238}\text{U}$  ages. The daughter  
370 isotopes of interest are those with longer half-lives, namely  $^{234}\text{U}$  and  $^{230}\text{Th}$ , both belonging to the  
371  $^{238}\text{U}$  decay chain. A deviation of 1 initial ( $^{234}\text{U}/^{238}\text{U}$ ) activity ratio ( $[\text{}^{234}\text{U}/^{238}\text{U}]_i$ ) unit from unity (e.g.  
372  $[\text{}^{234}\text{U}/^{238}\text{U}]_i = 0$ ) will cause an age difference of c. 354 ky and a deviation of 1  $[\text{}^{230}\text{Th}/^{238}\text{U}]_i$  will  
373 deviate our  $^{206}\text{Pb}^*/^{238}\text{U}$  dates by c. 109 ky (considering that secular equilibrium has been reached,  
374 calculated after Wendt and Carl, 1985).

375 Eight quartz clasts were cut in half to expose their silcrete coatings, mounted in epoxy mounts and  
376 polished at the Department of Geosciences, University of Cologne (UoC). U-Pb analyses were  
377 performed at the Goethe University Frankfurt (GUF) using a RESOLUTION 193 nm ArF excimer laser  
378 (COMpex Pro 102), equipped with a two-volume ablation cell (Laurin Technic S155). The laser  
379 was coupled to a ThermoScientific ElementXr sector field ICP-MS. The surfaces were cleaned with  
380 8 pre-ablation laser pulses. Ablation was carried out in a He (0.3 l/min), Ar (1.01 l/min) and N  
381 (0.012 l/min) atmosphere, with a high energy density (c. 5 J/cm<sup>2</sup>), a frequency of 15 Hz and round  
382 50 µm diameter spots (SI2\_Supporting Information).

383 Artificial silicate glasses NIST SRTM 612 and 614 were used as reference materials (RM). Plots  
384 and dates are calculated using the in-house spreadsheet program (Gerdes and Zeh, 2009, 2006),  
385 together with Isoplot (Ludwig, 2012). Ages are reported with and without systematic components  
386 (i.e., date ± 2s / 2s<sub>sys</sub>). Uncertainties include internal standard errors (SE), background, counting  
387 statistics, excess scatter of the primary reference material (NIST SRTM 612), and excess variance  
388 (calculated from NIST SRTM 614). Systematic uncertainties also propagate systematic errors,  
389 which are the long-term excess variance (1.5%, 2s), decay constant uncertainties (Horstwood et  
390 al., 2016) and the uncertainty derived from the initial activity ratio. Dates are calculated as Tera-



391 Wasserburg lower intercepts (Tera and Wasserburg, 1972). Linear regressions are anchored to a  
392 common-lead  $^{207}\text{Pb}/^{206}\text{Pb}$  ratio of 0.837. This is the Y-intercept of sample “DWA98008-Silc4 Black  
393 Crack”, which is where this ratio is better constrained. This value is in good agreement with  
394 modelled crustal values at the time of formation (0.836, Stacey and Kramers, 1975).

395 The samples dated are sufficiently old to have reached secular equilibrium and hence activity  
396 ratios cannot be measured (assuming a closed system behaviour). Consequently, the following  
397 initial activity ratios used are assumed. The silcretes dated in this study have virtually no Th  
398 (average of  $\sim 89$  ng/g) and therefore we consider  $[\text{}^{230}\text{Th}/\text{}^{238}\text{U}]_i = 0$  (initial  $^{230}\text{Th}/^{238}\text{U}$  activity  
399 ratio). Considering previous studies on calcretes and silcretes formed in semi-arid and arid  
400 environments (Oster et al., 2017; Maher et al., 2007; Neymark, 2011), the ground and surface  
401 waters from which these rocks are formed often have  $[\text{}^{234}\text{U}/\text{}^{238}\text{U}]_i$  values greater than 1. Therefore,  
402 the data in this study are calculated with  $[\text{}^{234}\text{U}/\text{}^{238}\text{U}]_i = 1.75 \pm 0.32$  (2s abs), which is a weighted  
403 average of the  $[\text{}^{234}\text{U}/\text{}^{238}\text{U}]_i$  of the above-mentioned studies. The uncertainty in this activity ratio is  
404 added to the final systematic uncertainties by quadratic propagation (Scardia et al., 2019;  
405 SI2\_Supporting Information).

#### 406 Cosmogenic $^{21}\text{Ne}$ Exposure Dating

407 We used prepared samples from Van Der Wateren and Dunai (2001) for in situ  $^{21}\text{Ne}$  exposure  
408 dating using the new noble gas mass spectrometer at the University of Cologne. The  $^{21}\text{Ne}$  analyses  
409 of Van Der Wateren and Dunai (2001) were performed without an international standard (CREU).  
410 For neon analysis we prepared amalgamated samples from each site containing between 35 and  
411 40 quartz clasts (100mg/sample) using the already prepared 63-125  $\mu\text{m}$  fraction. By also  
412 analysing shielded pebbles, a pre-exposure correction (accumulated  $^{21}\text{Ne}$  concentration during  
413 transport) can be applied to analysed surface samples (Repka et al., 1997). The presumably  
414 non-atmospheric  $^{21}\text{Ne}$  concentration found in these samples can be subtracted from the  
415 concentration in their exposed counterparts. The latter also corrects for any potential nucleogenic  
416  $^{21}\text{Ne}$  that may be present in the samples. Samples were measured on the noble gas mass  
417 spectrometer at the University of Cologne using the analytical methods outlined in Ritter et al.  
418 (2021). CREU quartz standards were measured in Cologne for interlaboratory comparability and  
419 quality control (Vermeesch et al., 2015). The spallogenic origin of the measured  $^{21}\text{Ne}$  excess was  
420 verified using the triple isotope plot.  $^{21}\text{Ne}$  exposure ages were calculated using the ‘nuclide  
421 dependent scaling’ after Lifton et al. (2014), calculated with “The online exposure age calculator  
422 formerly known as the CRONUS-Earth online exposure age calculator.” (Version 3,  
423 [http://hess.ess.washington.edu/math/v3/v3\\_age\\_in.html](http://hess.ess.washington.edu/math/v3/v3_age_in.html); Balco et al., 2008).



424 **5. Results**

425 Silcrete Imaging

426 Digital microscope images show vein-contact parallel-layering with different crystal orientation  
 427 (Fig. 4A). The Raman spectra peaks at 129, 209 and 467  $\text{cm}^{-1}$  are indicative for quartz, which  
 428 dominate the silcrete samples. Raman spectroscopy of DWA98008-Silc8 also indicate the  
 429 presence of one major calcite band (dark colour in Fig. 5B, Raman spectra peaks at 156, 283, 466,  
 430 714 and 1088  $\text{cm}^{-1}$ ). The calcite crack filling might be indicative for shattering of previous silcrete  
 431 and crack filling by repeated and/or ongoing calcrete formation within the Karpfenkliff  
 432 Conglomerate.

433 U-Pb Laser Ablation Results Silcrettes

434 Four out of the eight silcrete samples yielded meaningful dates (DWA98008 – Silc3, Silc4, Silc7,  
 435 Silc8), out of which 12 dates could be calculated (SI2\_Supporting Information). The dates range  
 436 from  $2.96 \pm 0.14$  to  $6.72 \pm 0.16$  Ma, with maximum relative abundance peaks at around 3.4 Ma and  
 437 about 5.5 Ma (see Fig. 6 and Table 1). All dates are calculated from multiple spot analyses, ranging  
 438 from 9 to 28 spots per date. The majority of the analyses have U concentrations between ~30 and  
 439 70  $\mu\text{g/g}$ , with an average of 42  $\mu\text{g/g}$ , and very low Th concentrations, up to 200  $\text{ng/g}$ , with an  
 440 average of 89  $\text{ng/g}$ .

441

Sample name	Date (Ma) <sup>(1)</sup>	2s abs <sup>(2)</sup>	2s sys <sup>(3)</sup>	Y-Intercept <sup>(4)</sup>	2s <sup>(5)</sup>	Anchored <sup>(6)</sup>	MSWD <sup>(7)</sup>	n <sup>(8)</sup> (used)	n <sup>(9)</sup> (total)	Date (Ma) <sup>(10)</sup>	2s abs <sup>(11)</sup>
Silc3 Rim 1	5.756	0.124	0.132	0.837	0.008	TRUE	0.45	9	9	5.590	0.120
Silc3 Rim 2	5.246	0.107	0.115	0.837	0.008	TRUE	0.41	9	9	5.080	0.103
Silc3 Rim 3	5.488	0.068	0.081	0.837	0.008	TRUE	1.35	24	28	5.322	0.066
Silc3 Rim Outer	3.734	0.064	0.071	0.838	0.011	TRUE	1.63	28	28	3.569	0.061
Silc4 Black crack	5.927	0.244	0.248	0.8374	0.0066	FALSE	1.50	21	25	5.761	0.237
Silc4 Rim	3.498	0.061	0.067	0.837	0.008	TRUE	1.24	16	17	3.332	0.058
Silc4 Rim Outer	3.456	0.061	0.067	0.837	0.008	TRUE	1.30	15	17	3.290	0.058
Silc4 Rim Inner	3.129	0.068	0.072	0.837	0.008	TRUE	1.63	9	9	2.964	0.064
Silc7	6.881	0.091	0.106	0.8528	0.0028	FALSE	0.94	27	29	6.715	0.089
Silc8 Rim Out 1	6.116	0.081	0.095	0.837	0.008	TRUE	0.64	20	20	5.950	0.079
Silc8 Rim Out 2	5.131	0.132	0.139	0.837	0.014	TRUE	2.56	17	25	4.965	0.128
Silc8 Rim Center	3.847	0.131	0.135	0.837	0.008	TRUE	1.37	20	20	3.681	0.126

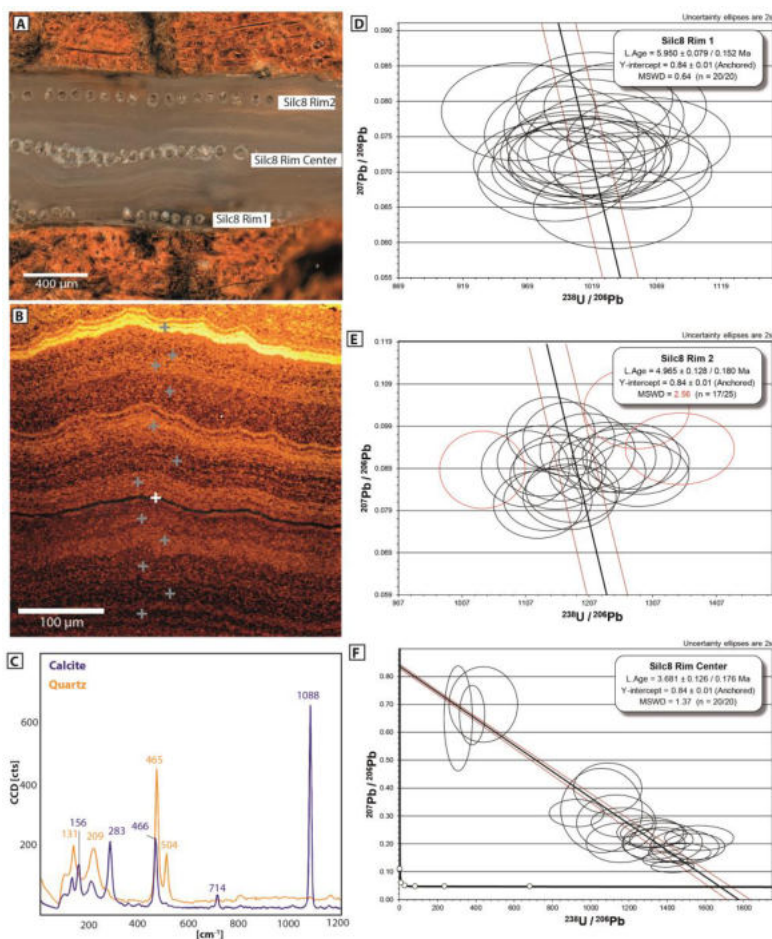
442

443 *Table 1: 1. - Concordia curve lower intercept dates, Tera-Wasserburg diagram (Tera and*  
 444 *Wasserburg, 1972). 2. - 2s absolute uncertainties, considering within-run precision (SE of the mean*  
 445 *of the ratios), excess of scatter, background, counting statistics and excess of variance (calculated*  
 446 *from the validating RM, SRTM NIST 614. 2.6%, 1s, on  $^{238}\text{U}/^{206}\text{Pb}$  and 0%, 1s, on  $^{207}\text{Pb}/^{206}\text{Pb}$  ratios).*  
 447 *3. - Previous uncertainties (2) expanded with systematic uncertainties (0.8 %, 2s, long term*  
 448 *reproducibility and decay constant uncertainties). See Horstwood et al. (2016). 4. -  $^{207}\text{Pb}/^{206}\text{Pb}$  ratio*  
 449 *of the upper intercept. 5. - 2s absolute uncertainty of the upper intercept. 6. - Whether or not the*  
 450 *linear regression on the Tera-Wasserburg is anchored. 7. - Mean squared weighted deviates of the*  
 451 *regression line. 8. - Number of analyses considered. 9. - Total number of analyses. 10. - Dates*  
 452 *calculated (following Wendt and Carl, 1985) considering an initial  $^{234}\text{U}/^{238}\text{U}$  activity ratio of 1.75,*  
 453 *and initial  $^{230}\text{U}/^{238}\text{U}$  activity ratios of 0. 11. - Uncertainties (2) recalculated to the new dates (10). 11. -*



454 *Uncertainties (3) recalculated to the new dates (10) and adding  $^{234}\text{U}/^{238}\text{U}$  activity ratio uncertainty*  
455 *(0.32, 2s abs).*

456



457

458 *Fig. 4: (A) Microscope image of sample DWA98008-Silc8 after LA-ICP-MS analysis. Laser spots are*  
459 *visible, respective U-Pb Tera-Wasserburg plots are shown in (D-F). (B) Raman image of Silc8, area*  
460 *not visible on microscope image. Grey crosses indicate measured quartz spectra. White cross marked*  
461 *the occurrence of Calcite, which can be traced as a black line. Raman imaging shows multiple*  
462 *layering of silcrete filling the crack of the shattered quartz clast. Color variations are indicative of*  
463 *differences in crystal orientations (C) Respective Raman spectra for the quartz and calcite*  
464 *identification. (D-F) Tera-Wasserburg plots of Silc8 and respective U-Pb ages (red ellipses are*  
465 *considered outliers).*

#### 466 TCN Exposure Age Results

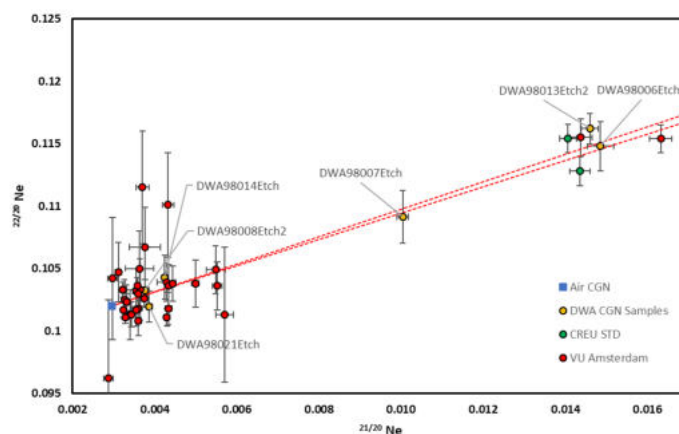
467  $^{21}\text{Ne}$  samples measured at the Noble Gas Laboratory in Cologne (Ritter et al., 2021) yield  
468 concentrations of  $1.52 - 1.95 \times 10^7$  atoms/gr for shielded samples (DWA98008, 014, 021) and  
469  $6.30 - 9.60 \times 10^7$  atoms/gr for surface samples (DWA98006,007, 013). All samples are within 2





470 sigma of the spallation line (Fig. 5). Compared to the  $^{21}\text{Ne}$  concentrations of Van Der Wateren and  
471 Dunai (2001), the etched samples measured in Cologne reveal lower concentrations of up to 13%  
472 difference when comparing direct concentrations (average of five measured samples), however,  
473 within  $\pm 1\sigma$  it reduces to  $\sim 1.6\%$ , agreeing within  $\pm 2\sigma$  on average. We have excluded sample  
474 DWA98008, as it presumably contains a high abundance of non-cosmogenic Ne, as deduced from  
475 the significant concentration differences between the sample measured by Van Der Wateren and  
476 Dunai (2001) and the etched counterpart measured in Cologne (SI1\_Supporting Information).  
477 Similar results and interpretations for sample DWA98008 were reported by Van Der Wateren and  
478 Dunai (2001).

479 Using the mean difference of  $\sim 13\%$  between VU Amsterdam and Cologne Ne concentrations  
480 (SI1\_Supporting Information), the data from Van Der Wateren and Dunai (2001) can be corrected  
481 for lab-specific differences. The corrected exposure ages are given in Table 2.



482

483 *Fig. 5: Triple isotope diagram indicating single-heat-step extraction of the Cologne laboratory*  
484 *(orange circles) compared to the multiple-heat-step extraction (red circles) of Van Der Wateren and*  
485 *Dunai (2001). Uncertainties are  $1\sigma$ . The red stippled line indicates the Cologne laboratory spallation*  
486 *line (Ritter et al., 2021). Green circles indicate CREU1 measured during the analysis in Cologne.*

487 Calculated exposure ages derived from Cronus Earth (Balco et al., 2008) are summarised in  
488 Table 2. For the Kuiseb terrace,  $^{21}\text{Ne}$  concentrations in shielded, pre-exposed samples  
489 (DWA98008, DWA98021), give a mean apparent age of  $0.65 \pm 0.04$  Ma (external uncertainty  $\pm 1\sigma$ ).  
490 The latter indicates that the non-cosmogenic component of DWA98008 has been removed by  
491 etching, indicating the identical apparent exposure age as DWA98021. Correction of the  $^{21}\text{Ne}$   
492 concentration of exposed rounded pebbles (DWA98007) from the top of the Carp Cliff terrace  
493 yields an exposure age of  $3.2 \pm 0.2$  Ma ( $\pm 1\sigma$  external uncertainty), being slightly older than  
494 calculated by Van Der Wateren and Dunai (2001), however, identical within the uncertainty.



495 Exposed angular clasts (DWA98006) show a younger exposure age of  $2.85 \pm 0.19$  Ma ( $\pm 1\sigma$  external  
496 uncertainty). The latter is slightly older than in Van Der Wateren and Dunai (2001), which is  
497 identical within their uncertainty. A similar exposure age of  $2.75 \pm 0.18$  Ma ( $\pm 1\sigma$  external  
498 uncertainty) was derived from angular clasts from the Kamberg cliff (DWA98013) with. Angular  
499 clasts are assumed to be derived from local sources without significant pre-exposure from long  
500 transport times. Our results indicate that terrace abandonment and exposure to cosmic rays  
501 started at  $\sim 2.8$  Ma (Fig. 6).

502 Table 2: TCN exposure ages.

	LSDn Exposure Age		
	Age [Ma]	Int. Unc. [Ma]	Ext. Unc. [Ma]
DWA98006Etch2	2.85	0.07	0.19
DWA98007Etch	3.85	0.07	0.25
Corr. DWA98007Etch2	3.20	0.05	0.20
DWA98008Etch2	0.66	0.02	0.05
DWA98021Etch	0.65	0.02	0.04
DWA98013Etch2	2.75	0.05	0.18
DWA98014Etch	0.90	0.02	0.06
DWA98001VU	5.35	0.23	0.41
DWA98002VU	3.98	0.32	0.40
DWA98003VU	1.08	0.13	0.15
DWA98005VU	0.58	0.06	0.07
DWA98019VU	0.49	0.05	0.06
DWA98024VU	1.27	0.12	0.14

## 503 6. Interpretation and Discussion

504 Our U-Pb ages are stratigraphically in the correct order, with the oldest U-Pb ages at the contact  
505 between quartz clast and filled rock fracture and the youngest age in the centre of the filled  
506 fracture (Table 1, Fig. 4). Recurrent U-Pb ages underpin and mark the main phase of silcrete, i.e.  
507 calcrete, formation. Groundwater calcrete formation, i.e., microscale silcrete formation, within the  
508 sediments of the proto-Kuiseb canyon (Karpfenkliff Conglomerate) took place between the Late  
509 Miocene ( $\sim 7$  Ma) and the Late Pliocene ( $\sim 3$  Ma, Fig. 6). The U-Pb silcrete ages suggest either  
510 persistent or alternating periods of wetter climate for groundwater calcrete formation.

511 Based on the causal relationship between silcrete and calcrete formation, our U-Pb silcrete ages  
512 indicate that environmental and climatic conditions during the Pliocene were sufficient to allow  
513 for carbonate leaching, transport and calcrete formation within the coarse-grained Karpfenkliff  
514 Conglomerate. However, whether the sampled groundwater calcrete is identical or synchronous  
515 with the prominent Kamberg Calcrete can be questioned, but we can narrow down the timing of



516 major groundwater calcrete formation, previously assigned to the Late Miocene (Goudie et al.,  
517 2015; Ward, 1987) or Plio-Pleistocene (Pickford and Senut, 2000). Calcrete formation ceased  
518 during the Late Pliocene/Early Pleistocene by incision and groundwater lowering (Fig. 6).

519 Re-measured TCN  $^{21}\text{Ne}$  surface exposure ages from amalgamated quartz clasts agree with the  
520 derived U-Pb silcrete chronology and are younger than the youngest U-Pb silcrete age obtained  
521 (Fig. 6), i.e., in stratigraphically correct order. The surface exposure ages mark the abandonment  
522 of the fluvial terraces and the onset of the Kuiseb River incision at  $\sim 2.8$  Ma. The latter caused a  
523 groundwater lowering of the water table and the cessation of calcrete formation within the  
524 Karpfenkliff Conglomerate Formation. Re-measurements of the quartz clasts from the Oswater  
525 terrace downstream of the Karpfenkliff and Kamberg cliff sampling sites confirm the exposure  
526 ages previously obtained by Van Der Wateren and Dunai (2001). The exposure ages of the  
527 Karpfenkliff and Oswater terrace constrain the period of major canyon incision to  $\sim 2.8$  -1.3 Ma  
528 (Fig. 6).

529 With the aid of absolute U-Pb silcrete and surface exposure dating, it is now possible to redefine  
530 depositional ages or depositional periods for sediments in the Central Namib Desert, some of  
531 which are widely used as marker horizons. Our U-Pb silcrete ages constrain the timing of sediment  
532 deposition within the Kuiseb Canyon (Karpfenkliff Conglomerate Formation) to be older than  
533  $\sim 7$  Ma, as silcrete formation within the conglomerates postdates deposition thereof (Fig. 6). The  
534 incision age of the Proto-Kuiseb and the subsequent deposition by the Karpfenkliff Conglomerate  
535 as proposed by Miller et al. (2021) of  $\sim 5$  Ma, does not agree with our absolute U-Pb ages. If the  
536 relative biostratigraphic dating of Pickford and Senut (2000) is valid, the proto-Kuiseb canyon  
537 was filled by the Karpfenkliff Conglomerate Formation over a time period of up to 6-7 Ma  
538 (Diamantornis corbetti at Elim  $\sim 14$  -15 Ma, see Pickford and Senut, 2000). Verification and  
539 absolute direct dating of the Karpfenkliff Formation is still lacking and is a target for future studies.  
540 Our fluvial chronology substantially supports the chronological data obtained by Van Der Wateren  
541 and Dunai (2001).

#### 542 **Pliocene Calcrete Formation – Steady State Climate**

543 Our U-Pb ages indicate a relatively calm or transitional phase between aggradation and backfilling  
544 of the Proto-Kuiseb (and presumably other drainage systems such as the Swakop) and the  
545 renewed incision by the recent Kuiseb River, throughout the Pliocene. U-Pb ages of microscale  
546 silcrete from the same stratigraphic horizon indicate a long-term stable groundwater level, i.e. no  
547 significant aggradation or degradation.

548 As the formation of groundwater calcrete is generally restricted to specific environmental  
549 conditions, the existence and chronology of its formation in the Central Namib Desert now allows



550 us to relate these environmental conditions to specific episodes in the past and thus to obtain a  
551 better and partly more quantitative paleoclimate and environmental reconstruction of the  
552 Pliocene in the Central Namib Desert. However, specific ranges of precipitation are still being  
553 discussed, with the upper limit between 600 and 1000 mm/yr (Mack and James, 1994) and the  
554 lower limit as low as 50 mm/yr (Goudie, 1973; Retallack, 1994). Ward (1987) suggests seasonal  
555 precipitation of potentially 350-450 mm in the upper reaches of the Kuiseb for calcrete formation.  
556 We therefore interpret our U-Pb silcrete chronology as marking the transition of the mean annual  
557 precipitation (MAP) from the upper potential limit of approximately ~600 mm/yr or the lower  
558 potential limit of 50 mm/yr in the Kuiseb catchment during the Late Miocene. Whether there was  
559 a climate change from, or a return to, wetter conditions during the Pliocene cannot be determined  
560 from our U-Pb chronology. Calcrete formation ceased with the incision of the Kuiseb River and a  
561 significant lowering of the groundwater table.

562 Marine records off Namibia (Fig. 6, ODP 1081, Hoetzel et al., 2017) suggest a shift to more arid  
563 conditions over the course of the Mid to Late Miocene, controlled by a gradual increase in the  
564 upwelling activity of the Benguela Current, initiated by a strengthening of the meridional gradient.  
565 This shift is supported by pollen data (Hoetzel et al., 2015; Dupont et al., 2013), indicating the  
566 expansion of savanna grasslands (C4 expansion) in Namibia since ~8 Ma, with a subsequent shift  
567 during the Pliocene to more shrubland and desert vegetation (Hoetzel et al., 2015).  
568 Compound-specific hydrogen isotopes (ODP 1085, Dupont et al., 2013) indicate a change in the  
569 precipitation source from the Atlantic to the Indian Ocean since ~8 Ma (Dupont et al., 2013).  
570 Therefore, our U-Pb chronology of calcrete formation (~7-3 Ma) tracks the shift to more arid  
571 conditions with a corresponding reduction in the MAP to allow calcrete formation. Nevertheless,  
572 this transition and aridification of the Namib was slow, and regional SST records (ODP 1082,  
573 Etourneau et al., 2009; ODP 1081, Rosell-Melé et al., 2014, Fig. 6), as well as global paleoclimate  
574 records (benthic  $\delta^{18}O$ , Westerhold et al., 2020, Fig. 6) indicate a relatively stable climatic period.  
575 Rosell-Melé et al. (2014) proposed, based on their marine SST record off Namibia (ODP 1082),  
576 that the persistently warm Pliocene, with conditions analogue to a persistent Benguela 'El Niño',  
577 ended at the transition to the Pleistocene (Fig. 6).

#### 578 **Plio/Pleistocene Transition**

579 During the transition from the late Pliocene to the early Pleistocene, the Central Namib Desert  
580 underwent large-scale landscape rejuvenation with drainage reorganisation and incision. This is  
581 the same period, in which Miller et al. (2010) reconstructed the major desiccation of the Etosha  
582 paleolake (Fig. 6). Based on U-Pb calcrete ages from the Kalahari basin, Houben et al. (2020)  
583 proposed an intensification of arid conditions since ~3.8 Ma, older than our onset of more arid  
584 conditions in the Central Namib at around 3 Ma. Higher offshore sedimentation rates off Namibia



585 may be associated with increased input of terrestrial material (Dupont et al., 2005) due to incision  
586 of E-W flowing drainages into the Atlantic. The propagation of the Horingbaai fan-delta (between  
587 Omaruru and the Ugab river) occurred approximately at the same time (2.7 -2.4 Ma) according to  
588 Stollhofen et al. (2014), supporting the idea of large-scale landscape rejuvenation and incision of  
589 multiple E-W flowing drainages in the Namib Desert.

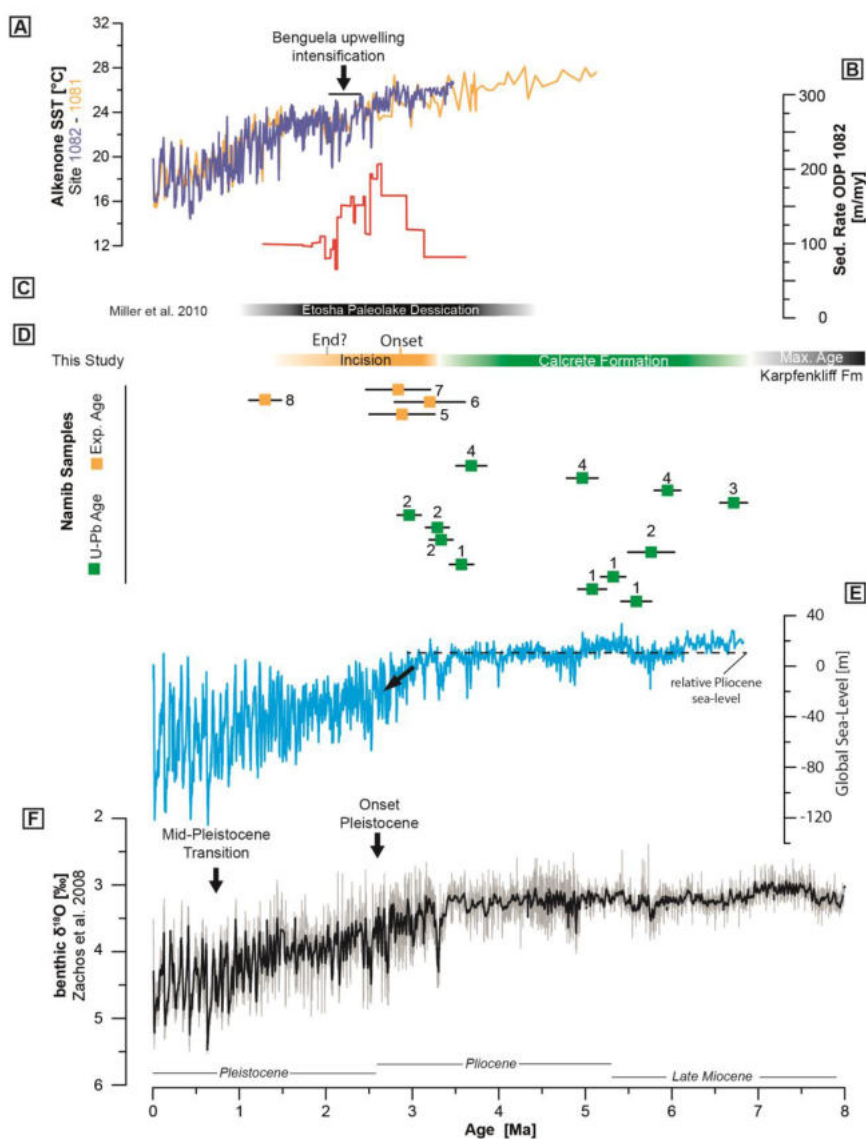
590 The underlying mechanism is still questionable, as several forcing factors could be responsible for  
591 the incision of major E-W flowing river systems: climate change and variability, sea level change  
592 and/or tectonic uplift. The latter was previously suggested by Ward (1987) and attributed to a  
593 late Neogene epeirogenic uplift. Stollhofen et al. (2014) also suggest that uplift could be one of the  
594 causes and/or at least a contributor to other factors, such as climate.

595 Data from the marine realm off Namibia suggest a further step towards more extreme arid  
596 conditions during the Plio-/Pleistocene transition (Fig. 6). Local SST records (ODP 1082,  
597 Etourneau et al., 2009; ODP 1081, Rosell-Melé et al., 2014, Fig. 6) indicate the onset of decreasing  
598 SSTs at ~2.7-2.5 Ma and the significant shift towards increased upwelling activity of colder water  
599 masses in the Benguela Current since ~2.2 Ma (Dupont et al., 2005; Marlow et al., 2000; Etourneau  
600 et al., 2009). The significant decrease in SSTs correlates with the further intensification of  
601 Northern Hemisphere glaciation since ~2.7 Ma (Ruggieri et al., 2009). The pollen record (ODP  
602 1082) of (Dupont, 2006) shows that arid to semi-arid biomes were rather limited prior to ~2.7  
603 Ma, and that their concentration increases with higher variability since then, reflecting the  
604 intensification of arid conditions in the Central Namib Desert (Dupont, 2006).

605 Vegetation change may be a major cause of the exposure of landscapes to accelerated erosion.  
606 Major river incision in the Central Namib Desert thus occurred during a period of climate change  
607 and greater climate variability compared to the more persistently stable Pliocene (Rosell-Melé et  
608 al., 2014), with the intensification of arid conditions in southern Africa, synchronous with major  
609 global changes. We therefore propose that the major river incision of the Kuiseb River at the  
610 Plio-/Pleistocene transition was caused by a shift to more arid conditions with decreasing  
611 precipitation, resulting in reduced river discharge, river steepening and incision (e.g. Whipple and  
612 Tucker, 1999; Bonnet and Crave, 2003). Catchment and river systems such as the Kuiseb (and/or  
613 river systems such as the Swakop), which had reached a steady-state during the more stable  
614 Pliocene, had to adapt to the new boundary conditions, which is in line with the global increase in  
615 erosion rates at the Plio-/Pleistocene transition (Herman et al., 2013; Herman and Champagnac,  
616 2016). A major vegetation shift towards more arid biomes and sparser vegetation cover increased  
617 the susceptibility of landscapes to erosion. The global sea-level drop at the Plio-/Pleistocene  
618 transition may have had an additional impact on drainage base levels.



619 The incision of the recent Kuiseb River can be constrained to a period between the derived terrace  
 620 ages of ~2.8 and ~1.3 Ma (minimum age of the Oswater bedrock river terrace). The actual period  
 621 of incision may be even shorter, given the cessation of fluvial sediment deposition offshore at  
 622 ~2 Ma (Dupont et al., 2005). Deposition of the Oswater Formation indicates a phase of  
 623 aggradation sometime after ~1.3 Ma, followed by an incision into the recent bed of the Kuiseb  
 624 River.



625

626 Fig. 6: Compilation of paleoclimate records. (A) Alkenone SSTs from ODP 1082 (Etourneau et al.,  
 627 2009) and ODP 1081 (Rosell-Melé et al., 2014). Intensification of Benguela upwelling according to



628 *Etourneau et al. (2009). (B) Sedimentation rate of ODP 1082 for the Plio/Pleistocene transition*  
629 *(Dupont, 2006). (C) Desiccation of the Etosha paleolake from Miller et al. (2010). (D) U-Pb silcrete*  
630 *and surface exposure ages (this study). Numbers indicate identical clasts. 1 - DWA98008-Silc3, 2 -*  
631 *DWA98008-Silc4, 3 - DWA98008-Silc7, 4 - DWA98008-Silc8, 5 - DWA98013, 6 - DWA98007, 7-*  
632 *DWA98006, 8 - DWA98024. (E) Global Sea-Level curve from Hansen et al. (2013). Black dashed line*  
633 *indicates relative mean sea-level during the Pliocene, followed by the global decrease since the Plio-*  
634 */Pleistocene transition. (F) Global Cenozoic reference benthic foraminifer oxygen isotope dataset*  
635 *(CENOGRID) from Westerhold et al. (2020).*

## 636 **Conclusion**

637 Our study demonstrates that microscale silcrete from the Central Namib Desert can be dated using  
638 U-Pb LA-ICP-MS, and that layered silcrete incrustations can be used as paleoclimate archives.  
639 LA-ICP-MS U-Pb dating of silcrete has advantages over bulk carbonate analysis because it is less  
640 affected by potential interferences and contamination. The combined dating approach with  
641 additional <sup>21</sup>Ne exposure age dating allows us to reconstruct major paleoclimate and landscape  
642 changes since the Late Miocene for the Central Namib Desert. We can corroborate previously  
643 obtained chronological data from Van Der Wateren and Dunai (2001) and place absolute age  
644 constraints on some sediments from the Central Namib Desert, some of which are used as marker  
645 horizons throughout the region. Our chronology of groundwater calcrete formation and river  
646 incision adds crucial information with absolute dates to the 'Namib Group'. Although specific  
647 precipitation ranges for calcrete formation are still being debated, we can assign potential  
648 precipitation ranges and their shifts to specific time episodes and thus provide a semi-quantitative  
649 picture of the aridification of the Central Namib Desert during the Late Miocene to the  
650 Plio-/Pleistocene. Our terrestrial paleoclimate record of microscale silcrete formation, i.e.,  
651 calcrete formation, supports the marine evidence for a persistently stable Pliocene climate in the  
652 Central Namib Desert. The cessation of groundwater calcrete formation was caused by the deep  
653 incision of the Kuiseb River (presumably synchronous with other E-W flowing drainage systems  
654 of the Central Namib Desert) at the Plio-/Pleistocene transition, which can be explained by the  
655 intensification of aridity, vegetation change, and presumably global sea-level drop. Global climate  
656 change with the onset of the Pleistocene was most likely the major forcing factor for major  
657 landscape rejuvenation and change in the Central Namib Desert. Precipitation decline in the  
658 Kuiseb River catchment is identified as the tipping point for the local climate and landscape  
659 response.

## 660 **Acknowledgements:**

661 We want to thank our colleagues from the Gobabeb Research Station for their help during  
662 fieldwork in 2018. Moreover, we want to thank our preparation workshops for preparation of thin  
663 sections and pucks. We also want to thank Prof. A. Woodland, for his support with Raman



664 spectroscopy. This project is affiliated with the Collaborative Research Center (CRC) 1211, funded  
665 by the German Science Foundation (DFG), Projektnummer 268236062. This is FIERCE  
666 contribution number XXX.

667 **Author Contribution:**

668 B.R. fieldwork, sample preparation, <sup>21</sup>Ne noble gas analytic, data evaluation, manuscript writing.  
669 R.A. U-Pb dating, sample analysis thin section, Raman, data analysis, manuscript writing. A.R.  
670 Raman, F.M.v.d.W. fieldwork, T.J.D. fieldwork, data evaluation. A.G. data analysis. All authors  
671 reviewed the manuscript.

672 **Additional Information**

673 **Declaration of interest:** The authors declare that the research was conducted in the absence of  
674 any commercial or financial relationships that could be construed as a potential conflict of  
675 interest.

676 **Data availability statement:** All data generated or analysed during this study are included in this  
677 published article (and its supporting information files).

678 **References**

679

680 Alonso-Zarza, A. M.: Palaeoenvironmental significance of palustrine carbonates and calcretes in  
681 the geological record, *Earth-Science Reviews*, 60, 261-298, 2003.

682

683 Alonso-Zarza, A. M. and Wright, V.: Calcretes, *Developments in Sedimentology*, 61, 225-267, 2010.

684

685 Balco, G., Stone, J. O., Lifton, N. A., and Dunai, T. J.: A complete and easily accessible means of  
686 calculating surface exposure ages or erosion rates from (10)Be and (26)Al measurements,  
687 *Quaternary Geochronology*, 3, 174-195, 10.1016/j.quageo.2007.12.001, 2008.

688

689 Bierman, P. R. and Caffee, M.: Slow rates of rock surface erosion and sediment production across  
690 the Namib Desert and escarpment, southern Africa, *Am. J. Sci.*, 301, 326-358, 2001.

691

692 Bonnet, S. and Crave, A.: Landscape response to climate change: Insights from experimental  
693 modeling and implications for tectonic versus climatic uplift of topography, *Geology*, 31, 123-126,  
694 2003.

695

696 Branca, M., Masi, U., and Voltaggio, M.: An unsuccessful attempt at U/Th dating of soil calcretes  
697 from the Doukkali area (western Morocco) and environmental implications, *Geochemistry*, 65,  
698 347-356, 2005.

699

700 Butt, C., Horwitz, R., and Mann, A.: Uranium occurrences in calcrete and associated sediments in  
701 Western Australia, Commonwealth Scientific and Industrial Research Organization, 1977.





- 702
- 703 Candy, I. and Black, S.: The timing of Quaternary calcrete development in semi-arid southeast  
704 Spain: investigating the role of climate on calcrete genesis, *Sedimentary Geology*, 218, 6-15, 2009.  
705
- 706 Candy, I., Black, S., and Sellwood, B. W.: Quantifying time scales of pedogenic calcrete formation  
707 using U-series disequilibria, *Sedimentary Geology*, 170, 177-187, 10.1016/j.sedgeo.2004.07.003,  
708 2004.  
709
- 710 Dupont, L. M.: Late Pliocene vegetation and climate in Namibia (southern Africa) derived from  
711 palynology of ODP site 1082, *Geochemistry Geophysics Geosystems*, 7, Q05007,  
712 doi:10.1029/102005GC001208, 2006.  
713
- 714 Dupont, L. M., Rommerskirchen, F., Mollenhauer, G., and Schefuß, E.: Miocene to Pliocene changes  
715 in South African hydrology and vegetation in relation to the expansion of C4 plants, *Earth and  
716 Planetary Science Letters*, 375, 408-417, 2013.  
717
- 718 Dupont, L. M., Donner, B., Vidal, L., Pérez, E. M., and Wefer, G.: Linking desert evolution and coastal  
719 upwelling: Pliocene climate change in Namibia, *Geology*, 33, 461-464, 2005.  
720
- 721 Etourneau, J., Martinez, P., Blanz, T., and Schneider, R.: Pliocene–Pleistocene variability of  
722 upwelling activity, productivity, and nutrient cycling in the Benguela region, *Geology*, 37, 871-874,  
723 2009.  
724
- 725 Geological Survey of Namibia: Geological Map 2314 Kuiseb 1:250 000 ESRI Shapefile, Geological  
726 Survey of Namibia, Windhoek, Geological Series, 2016.  
727
- 728 Gerdes, A. and Zeh, A.: Combined U–Pb and Hf isotope LA-(MC-) ICP-MS analyses of detrital  
729 zircons: comparison with SHRIMP and new constraints for the provenance and age of an  
730 Armorican metasediment in Central Germany, *Earth and Planetary Science Letters*, 249, 47-61,  
731 2006.  
732
- 733 Gerdes, A. and Zeh, A.: Zircon formation versus zircon alteration—new insights from combined U–  
734 Pb and Lu–Hf in-situ LA-ICP-MS analyses, and consequences for the interpretation of Archean  
735 zircon from the Central Zone of the Limpopo Belt, *Chemical Geology*, 261, 230-243, 2009.  
736
- 737 Geyh, M. A. and Eitel, B.: Radiometric dating of young and old calcrete, *Radiocarbon*, 40, 795-802,  
738 1997.  
739
- 740 Goudie, A.: Duricrusts in tropical and subtropical landscapes, *Duricrusts in Tropical and  
741 Subtropical Landscapes*, 1973.  
742
- 743 Goudie, A.: Organic agency in calcrete development, *Journal of Arid Environments*, 32, 103-110,  
744 1996.  
745
- 746 Goudie, A.: Duricrusts and landforms, in: *Geomorphology and soils*, Routledge, 37-57, 2020.  
747



- 748 Goudie, A. and Viles, H.: Landscapes and landforms of Namibia, Springer2014.  
749
- 750 Goudie, A., Viles, H., Goudie, A., and Viles, H.: Calcretes: The Kamberg Calcrete Formation and the  
751 Karpencliff Conglomerate, Landscapes and Landforms of Namibia, 111-114, 2015.  
752
- 753 Hansen, J., Sato, M., Russell, G., and Kharecha, P.: Climate sensitivity, sea level and atmospheric  
754 carbon dioxide, Philosophical Transactions of the Royal Society A: Mathematical, Physical and  
755 Engineering Sciences, 371, 20120294, 2013.  
756
- 757 Herman, F. and Champagnac, J. D.: Plio-Pleistocene increase of erosion rates in mountain belts in  
758 response to climate change, Terra Nova, 28, 2-10, 2016.  
759
- 760 Herman, F., Seward, D., Valla, P. G., Carter, A., Kohn, B., Willett, S. D., and Ehlers, T. A.: Worldwide  
761 acceleration of mountain erosion under a cooling climate, Nature, 504, 423-426, 2013.  
762
- 763 Hoetzel, S., Dupont, L. M., and Wefer, G.: Miocene–Pliocene vegetation change in south-western  
764 Africa (ODP Site 1081, offshore Namibia), Palaeogeography, Palaeoclimatology, Palaeoecology,  
765 423, 102-108, 2015.  
766
- 767 Hoetzel, S., Dupont, L. M., Marret, F., Jung, G., and Wefer, G.: Steps in the intensification of Benguela  
768 upwelling over the Walvis Ridge during Miocene and Pliocene, International Journal of Earth  
769 Sciences, 106, 171-183, 2017.  
770
- 771 Horstwood, M. S., Košler, J., Gehrels, G., Jackson, S. E., McLean, N. M., Paton, C., Pearson, N. J.,  
772 Sircombe, K., Sylvester, P., and Vermeesch, P.: Community-derived standards for LA-ICP-MS U-  
773 (Th-) Pb geochronology–Uncertainty propagation, age interpretation and data reporting,  
774 Geostandards and Geoanalytical Research, 40, 311-332, 2016.  
775
- 776 Houben, G. J., Kaufhold, S., Miller, R. M., Lohe, C., Hinderer, M., Noll, M., Hornung, J., Joseph, R.,  
777 Gerdes, A., and Sitnikova, M.: Stacked megafans of the Kalahari Basin as archives of  
778 paleogeography, river capture, and Cenozoic paleoclimate of southwestern Africa, Journal of  
779 Sedimentary Research, 90, 980-1010, 2020.  
780
- 781 Jacobson, P. J., Jacobson, K. M., and Seely, M. K.: Ephemeral rivers and their catchments: Sustaining  
782 people and development in Namibia, Desert Research Foundation of Namibia, Windhoek, 160  
783 pp.1995.  
784
- 785 Kelly, M., Black, S., and Rowan, J.: A calcrete-based U/Th chronology for landform evolution in the  
786 Sorbas basin, southeast Spain, Quaternary Science Reviews, 19, 995-1010, 2000.  
787
- 788 King, L.: The geomorphology of the Eastern and Southern districts of Southern Rhodesia, South  
789 African Journal of Geology, 54, 33-64, 1951.  
790
- 791 King, L. C.: Pediplanation and isostasy: an example from South Africa, Quarterly Journal of the  
792 Geological Society, 111, 353-359, 1955.  
793



- 794 Korn, H. and Martin, H.: The Pleistocene in South West Africa, Proceedings of the 3rd Pan-African  
795 Congress on Prehistory, 14-22,  
796
- 797 Lancaster, N.: Palaeoenvironments in the Tsondab valley, Central Namib desert, in: Palaeoecology  
798 of Africa and of the Surrounding Islands and Antarctica, edited by: Coetzee, J. A., and van Zinderen  
799 Bakker, E. M., Balkema, Cape Town, 411-419, 1984.  
800
- 801 Lifton, N., Sato, T., and Dunai, T. J.: Scaling in situ cosmogenic nuclide production rates using  
802 analytical approximations to atmospheric cosmic-ray fluxes, *Earth and Planetary Science Letters*,  
803 386, 149-160, 10.1016/j.epsl.2013.10.052, 2014.  
804
- 805 Ludwig, K. R.: User's manual for Isoplot 3.75., Berkeley Geochronological Center Special  
806 Publication No. 5., 2012.  
807
- 808 Mack, G. H. and James, W.: Paleoclimate and the global distribution of paleosols, *The Journal of*  
809 *Geology*, 102, 360-366, 1994.  
810
- 811 Maher, K., Wooden, J., Paces, J., and Miller, D.:  $^{230}\text{Th}$ -U dating of surficial deposits using the ion  
812 microprobe (SHRIMP-RG): A microstratigraphic perspective, *Quaternary International*, 166, 15-  
813 28, 2007.  
814
- 815 Mann, A. and Horwitz, R.: Groundwater calcrete deposits in Australia some observations from  
816 Western Australia, *Journal of the Geological Society of Australia*, 26, 293-303, 1979.  
817
- 818 Marlow, J. R., Lange, C. B., Wefer, G., and Rosell-Melé, A.: Upwelling intensification as part of the  
819 Pliocene-Pleistocene climate transition, *Science*, 290, 2288-2291, 2000.  
820
- 821 McBride, E. F.: Quartz cement in sandstones: a review, *Earth-Science Reviews*, 26, 69-112, 1989.  
822
- 823 Miller, R.: The Geology of Namibia, Ministry of Mines and Energy - Geological Survey Namibia, 3,  
824 25-21, 2008.  
825
- 826 Miller, R. M., Pickford, M., and Senut, B.: The geology, palaeontology and evolution of the Etosha  
827 Pan, Namibia: Implications for terminal Kalahari deposition, *South African Journal of Geology*,  
828 113, 307-334, 2010.  
829
- 830 Miller, R. M., Krapf, C., Hoey, T., Fitchett, J., Ngungo, A.-K., Muyambas, R., Ndeutepo, A., Medialdea,  
831 A., Whitehead, A., and Stengel, I.: A sedimentological record of fluvial-aeolian interactions and  
832 climate variability in the hyperarid northern Namib Desert, Namibia, *South African Journal of*  
833 *Geology*, 124, 575-610, 2021.  
834
- 835 Milnes, A. and Thiry, M.: Silcretes, in: *Developments in earth surface processes*, Elsevier, 349-377,  
836 1992.  
837



- 838 Milnes, A., Wright, M., and Thiry, M.: Silica accumulations in saprolites and soils in South Australia,  
839 Occurrence, characteristics, and genesis of carbonate, gypsum, and silica accumulations in soils,  
840 26, 121-149, 1991.  
841
- 842 Nash, D. J. and Shaw, P. A.: Silica and carbonate relationships in silcrete-calcrete intergrade  
843 duricrusts from the Kalahari of Botswana and Namibia, *Journal of African Earth Sciences*, 27, 11-  
844 25, 1998.  
845
- 846 Nash, D. J. and Smith, R. F.: Multiple calcrete profiles in the Tabernas Basin, southeast Spain: their  
847 origins and geomorphic implications, *Earth Surface Processes and Landforms: The Journal of the*  
848 *British Geomorphological Group*, 23, 1009-1029, 1998.  
849
- 850 Netterberg, F.: The interpretation of some basic calcrete types, *The South African Archaeological*  
851 *Bulletin*, 24, 117-122, 1969.  
852
- 853 Neymark, L.: Potential effects of alpha-recoil on uranium-series dating of calcrete, *Chemical*  
854 *Geology*, 282, 98-112, 2011.  
855
- 856 Neymark, L.: Uranium-Lead dating, opal, 2014.  
857
- 858 Ollier, C.: Outline geological and geomorphic history of the central Namib Desert, Madoqua, 1977,  
859 207-212, 1977.  
860
- 861 Oster, J. L., Kitajima, K., Valley, J. W., Rogers, B., and Maher, K.: An evaluation of paired  $\delta^{18}O$  and  
862  $(^{234}U/^{238}U)$  0 in opal as a tool for paleoclimate reconstruction in semi-arid environments,  
863 *Chemical Geology*, 449, 236-252, 2017.  
864
- 865 Partridge, T. and Maud, R.: Geomorphic evolution of southern Africa since the Mesozoic, *South*  
866 *African Journal of Geology*, 90, 179-208, 1987.  
867
- 868 Pickford, M. and Senut, B.: Geology and Palaeobiology of the Central and Southern Namib Desert,  
869 Southwestern Africa: Geology and History of Study, Geological Survey 2000.  
870
- 871 Pickford, M., Senut, B., and Dauphin, Y.: Biostratigraphy of the Tsondab sandstone (Namibia) based  
872 on gigantic avian eggshells, *Geobios*, 28, 85-98, 1995.  
873
- 874 Pickford, M., Senut, B., Gommery, D., Andrews, P., and Banham, P.: Sexual dimorphism in  
875 *Morotopithecus bishopi*, an early Middle Miocene hominoid from Uganda, Late Cenozoic  
876 environments and hominid evolution: a tribute to Bill Bishop, 27-38, 1999.  
877
- 878 Rasbury, E. T. and Cole, J. M.: Directly dating geologic events: U-Pb dating of carbonates, *Reviews*  
879 *of Geophysics*, 47, 2009.  
880
- 881 Repka, J. L., Anderson, R. S., and Finkel, R. C.: Cosmogenic dating of fluvial terraces, Fremont River,  
882 Utah, *Earth and Planetary Science Letters*, 152, 59-73, [http://dx.doi.org/10.1016/S0012-821X\(97\)00149-0](http://dx.doi.org/10.1016/S0012-821X(97)00149-0), 1997.  
883



- 884
- 885 Retallack, G. J.: The environmental factor approach to the interpretation of paleosols, Factors of  
886 soil formation: A fiftieth anniversary retrospective, 33, 31-64, 1994.  
887
- 888 Richards, K. and Richards, K.: River channels: environment and process, Basil Blackwell 1987.  
889
- 890 Ritter, B., Vogt, A., and Dunai, T. J.: Technical Note: Noble gas extraction procedure and  
891 performance of the Cologne Helix MC Plus multi-collector noble gas mass spectrometer for  
892 cosmogenic neon isotope analysis, *Geochronology*, 2021, 2021.  
893
- 894 Rosell-Melé, A., Martínez-García, A., and McClymont, E. L.: Persistent warmth across the Benguela  
895 upwelling system during the Pliocene epoch, *Earth and Planetary Science Letters*, 386, 10-20,  
896 2014.  
897
- 898 Ruggieri, E., Herbert, T., Lawrence, K. T., and Lawrence, C. E.: Change point method for detecting  
899 regime shifts in paleoclimatic time series: application to  $\delta^{18}O$  time series of the Plio-Pleistocene,  
900 *Paleoceanography*, 24, 2009.  
901
- 902 Rutter, E.: Pressure solution in nature, theory and experiment, *Journal of the Geological Society*,  
903 140, 725-740, 1983.  
904
- 905 Scardia, G., Parenti, F., Miggins, D. P., Gerdes, A., Araujo, A. G., and Neves, W. A.: Chronologic  
906 constraints on hominin dispersal outside Africa since 2.48 Ma from the Zarqa Valley, Jordan,  
907 *Quaternary Science Reviews*, 219, 1-19, 2019.  
908
- 909 Senut, B.: Fossil ratite eggshells: a useful tool for Cainozoic biostratigraphy in Namibia,  
910 *Communications of the geological Survey of Namibia*, 12, 367-373, 2000.  
911
- 912 Sorby, H. C.: II. The Bakerian lecture.—On the direct correlation of mechanical and chemical forces,  
913 *Proceedings of the Royal Society of London*, 538-550, 1863.  
914
- 915 Stacey, J. t. and Kramers, J.: Approximation of terrestrial lead isotope evolution by a two-stage  
916 model, *Earth and planetary science letters*, 26, 207-221, 1975.  
917
- 918 Stokes, M., Nash, D. J., and Harvey, A. M.: Calcrete 'fossilisation' of alluvial fans in SE Spain: The roles  
919 of groundwater, pedogenic processes and fan dynamics in calcrete development, *Geomorphology*,  
920 85, 63-84, 2007.  
921
- 922 Stollhofen, H., Stanistreet, I. G., von Hagke, C., and Nguno, A.: Pliocene–Pleistocene climate change,  
923 sea level and uplift history recorded by the Horingbaai fan-delta, NW Namibia, *Sedimentary  
924 geology*, 309, 15-32, 2014.  
925
- 926 Stone, A.: Age and dynamics of the Namib Sand Sea: A review of chronological evidence and  
927 possible landscape development models, *Journal of African Earth Sciences*, 82, 70-87, 2013.  
928



- 929 Summerfield, M.: Silcrete as a palaeoclimatic indicator: evidence from southern Africa,  
930 Palaeogeography, Palaeoclimatology, Palaeoecology, 41, 65-79, 1983a.  
931
- 932 Summerfield, M. A.: Petrography and diagenesis of silcrete from the Kalahari Basin and Cape  
933 coastal zone, Southern Africa, Journal of Sedimentary Research, 53, 895-909, 1983b.  
934
- 935 Taylor, G. and Eggleton, R.: Silcrete: an Australian perspective, Australian Journal of Earth  
936 Sciences, 64, 987-1016, 2017.  
937
- 938 Tera, F. and Wasserburg, G.: U-Th-Pb systematics in lunar highland samples from the Luna 20 and  
939 Apollo 16 missions, Earth and Planetary Science Letters, 17, 36-51, 1972.  
940
- 941 Van der Wateren, F. M. and Dunai, T. J.: Late Neogene passive margin denudation history -  
942 cosmogenic isotope measurements from the central Namib desert, Global and Planetary Change,  
943 30, 271-307, 10.1016/s0921-8181(01)00104-7, 2001.  
944
- 945 Vermeesch, P., Fenton, C., Kober, F., Wiggs, G., Bristow, C. S., and Xu, S.: Sand residence times of one  
946 million years in the Namib Sand Sea from cosmogenic nuclides, Nature Geoscience, 3, 862-865,  
947 2010.  
948
- 949 Vermeesch, P., Balco, G., Blard, P. H., Dunai, T. J., Kober, F., Niedermann, S., Shuster, D. L., Strasky,  
950 S., Stuart, F. M., Wieler, R., and Zimmermann, L.: Interlaboratory comparison of cosmogenic Ne-21  
951 in quartz, Quaternary Geochronology, 26, 20-28, doi.org/10.1016/j.quageo.2012.11.009, 2015.  
952
- 953 Ward, J. and Corbett, I.: Towards an age for the Namib, Namib ecology, 25, 17-26, 1990.  
954
- 955 Ward, J. D.: The Cenozoic succession in the Kuiseb valley, central Namib desert, Geological Survey  
956 of Namibia Memoir, Windhoek 1987.  
957
- 958 Ward, J. D., Seely, M. K., and Lancaster, N.: On the antiquity of the Namib, South African Journal of  
959 Science, 79, 175-183, 1983.  
960
- 961 Weissel, J. K. and Seidl, M. A.: Inland propagation of erosional escarpments and river profile  
962 evolution across the southeast Australian passive continental margin, Geophysical Monograph-  
963 American Geophysical Union, 107, 189-206, 1998.  
964
- 965 Wendt, I. and Carl, C.: U/Pb dating of discordant 0.1 Ma old secondary U minerals, Earth and  
966 Planetary Science Letters, 73, 278-284, 1985.  
967
- 968 Westerhold, T., Marwan, N., Drury, A. J., Liebrand, D., Agnini, C., Anagnostou, E., Barnet, J. S., Bohaty,  
969 S. M., De Vleeschouwer, D., and Florindo, F.: An astronomically dated record of Earth's climate and  
970 its predictability over the last 66 million years, Science, 369, 1383-1387, 2020.  
971
- 972 Whipple, K. X. and Tucker, G. E.: Dynamics of the stream-power river incision model: Implications  
973 for height limits of mountain ranges, landscape response timescales, and research needs, Journal  
974 of Geophysical Research: Solid Earth, 104, 17661-17674, 1999.



- 975
- 976 Wilson, M. J.: Dissolution and formation of quartz in soil environments: A review, *Soil Sci. Annu.*,  
977 71, 3-14, 2020.  
978
- 979 Yaalon, D. H. and Ward, J. D.: Observations on calcrete and recent calcic horizons in relation to  
980 landforms, central Namib desert, in: *Palaeoecology of Africa and of the Surrounding Islands and*  
981 *Antarctica*, edited by: Coetzee, J. A., and van Zinderen Bakker, E. M., Balkema, Cape Town, 183-186,  
982 1982.
- 983 Candy, I., Black, S., 2009. The timing of Quaternary calcrete development in semi-arid southeast  
984 Spain: Investigating the role of climate on calcrete genesis. *Sedimentary Geology* 218, 6–15.  
985 <https://doi.org/10.1016/j.sedgeo.2009.03.005>
- 986 Maher, K., Wooden, J.L., Paces, J.B., Miller, D.M., 2007.  $^{230}\text{Th}$ -U dating of surficial deposits using  
987 the ion microprobe (SHRIMP-RG): A microstratigraphic perspective. *Quaternary International*,  
988 *Dating Quaternary sediments and landforms in Drylands* 166, 15–28.  
989 <https://doi.org/10.1016/j.quaint.2007.01.003>
- 990 Neymark, L., 2015. Uranium–Lead Dating, Opal. [https://doi.org/10.1007/978-94-007-6326-](https://doi.org/10.1007/978-94-007-6326-5_263-1)  
991 [5\\_263-1](https://doi.org/10.1007/978-94-007-6326-5_263-1)
- 992 Neymark, L.A., 2011. Potential effects of alpha-recoil on uranium-series dating of calcrete.  
993 *Chemical Geology* 282, 98–112. <https://doi.org/10.1016/j.chemgeo.2011.01.013>
- 994 Neymark, L.A., Amelin, Y., Paces, J.B., Peterman, Z.E., 2002. U-Pb ages of secondary silica at Yucca  
995 Mountain, Nevada: implications for the paleohydrology of the unsaturated zone. *Applied*  
996 *Geochemistry* 17, 709–734. [https://doi.org/10.1016/S0883-2927\(02\)00032-X](https://doi.org/10.1016/S0883-2927(02)00032-X)
- 997 Neymark, L.A., Amelin, Y.V., Paces, J.B., 2000.  $^{206}\text{Pb}$ – $^{230}\text{Th}$ – $^{234}\text{U}$ – $^{238}\text{U}$  and  $^{207}\text{Pb}$ – $^{235}\text{U}$   
998 geochronology of Quaternary opal, Yucca Mountain, Nevada. *Geochimica et Cosmochimica Acta*  
999 64, 2913–2928. [https://doi.org/10.1016/S0016-7037\(00\)00408-7](https://doi.org/10.1016/S0016-7037(00)00408-7)
- 1000 Oster, J.L., Kitajima, K., Valley, J.W., Rogers, B., Maher, K., 2017. An evaluation of paired  $\delta^{18}\text{O}$  and  
1001 ( $^{234}\text{U}/^{238}\text{U}$ )<sub>0</sub> in opal as a tool for paleoclimate reconstruction in semi-arid environments.  
1002 *Chemical Geology* 449, 236–252. <https://doi.org/10.1016/j.chemgeo.2016.12.009>
- 1003 Scardia, G., Parenti, F., Miggins, D.P., Gerdes, A., Araujo, A.G.M., Neves, W.A., 2019. Chronologic  
1004 constraints on hominin dispersal outside Africa since 2.48 Ma from the Zarqa Valley, Jordan.  
1005 *Quaternary Science Reviews* 219, 1–19. <https://doi.org/10.1016/j.quascirev.2019.06.007>
- 1006